Supplementary Information

Electrophoresis Assisted Printing: a Method to Control the Morphology in Organic Thin Films

*Stephan Pröller[a], Oliver Filonik[a], Fabian Eller[b], Salma Mansi[a], Chenhui Zhu[c], Eric Schaible[c], Alexander Hexemer[c], Peter Müller-Buschbaum[d,e], and Eva M. Herzig[a,b,]**

[a]Technische Universität München, Munich School of Engineering, Herzig Group, Lichtenbergstr. 4a, 85748 Garching, Germany

[b]Universität Bayreuth, Physikalisches Institut, Dynamik und Strukturbildung - Herzig Group, Universitätsstr. 30, 95447 Bayreuth, Germany

[c]Lawrence Berkeley National Laboratory, Advanced Light Source, CA 94720 Berkeley, California, USA

[d]Technische Universität München, Physik-Department, Lehrstuhl für Funktionelle Materialien, James-Franck-Str. 1, 85748 Garching, Germany

[e]Heinz Maier-Leibnitz-Zentrum, Lichtenbergstr. 1, 85748 Garching, Germany

* Email: Eva.Herzig@uni-bayreuth.de

Figure S 1 shows averaged solar cell parameters averaged over three independent batches of solar cells. The power conversion efficiency is improved by 25 % compared to the reference cell upon application of a high backward electric field during printing. The main driving parameters are the short circuit current (increase by 10 %) and the fill factor (increase by 15 %). The error bars are calculated using an error propagation from each individual batch and its standard deviation.

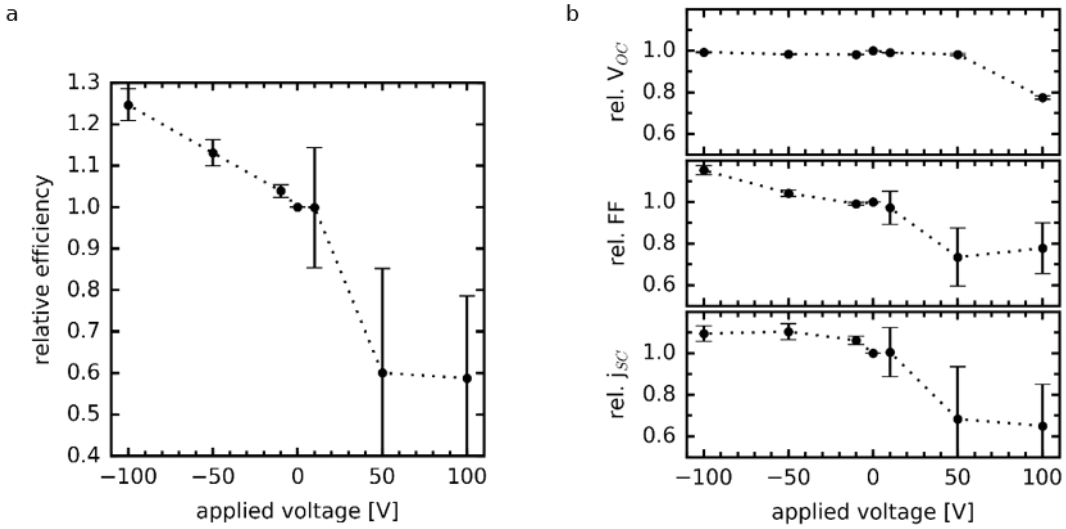

Figure S 1: Averaged, normalized solar cell parameters. Relative solar cell parameters of ITO/PEDOT:PSS/P3HT:PCBM (1:1)/Al devices for different applied voltages between print head/top electrode and the ITO. The (**a**) power conversion efficiency and (**b**) open circuit voltage (V_{OC}), fill factor (FF) and short circuit current density (j_{SC}) are each normalized to the reference device printed without application of an external electric field. The error bars result from averaging over three batches of solar cells. For comparing the influence, the parameters on the right hand side are plotted with equal ordinate range. The dotted lines are guides to the eye.

To confirm the functionality of the polymer after the treatment with an external electric field and voltages up to 100 V, we performed absorption measurements, which are depicted in **Figure S 2.** An indication of the non-destructive intervention of the electric field was already given by the preserved open circuit voltage of the devices fabricated under the electric field. Further to that, the absorbance of all printed films exhibits the same typical features for P3HT:PCBM blends, namely the 0-0 transition at around 600 nm and the 0-1 and 0-2 absorption bands at around 550 nm and 510 nm.

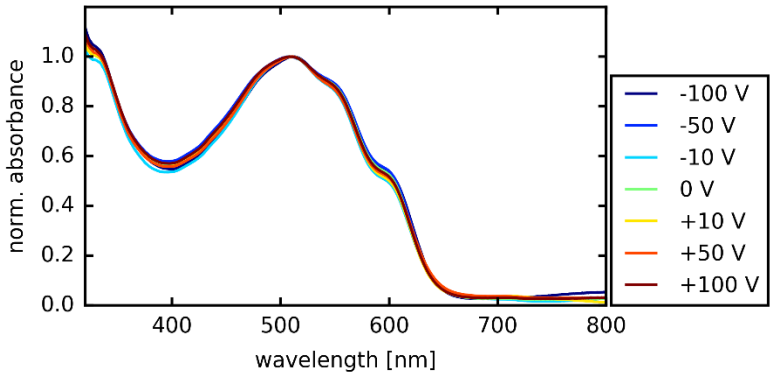

Figure S 2: Absorbance spectra of P3HT:PCBM films. The spectra of the films printed under different applied voltages between print head/top electrode and the ITO normalized to the main absorption peak.

To obtain information about the crystal structure of the films, grazing incidence wide angle X-ray scattering (GIWAXS) is performed [1]. In **Figure S 3**, an exemplary 2-dimensional scattering pattern is shown after conversion into momentum space using the software GIXSGUI [21]. At q = 0 Å^{-1}, a beam stop is blocking the direct beam and part of the grazing incidence small angle X-ray scattering (GISAXS) signal. The typically found crystal orientations [3] in a poly(3-hexylthiophene) (P3HT) film are schematically shown in **Figure S 3**. A scattering signal from the (100)-planes of the backbone spacing is found at $|q| \approx 0.38$ Å^{-1} in good agrement with literature [4,5]. For an edge-on oriented crystal the (100)-planes are parallel to the substrate and the [100]–direction perpendicular to the substrate. Thus, a pronounced scattering is found in the scattering pattern in vertical direction at $q_z \approx 0.38$ Å^{-1}. Similarly, for the face-on oriented crystals, which exhibit the (100)-planes perpendicular to the substrate and the [100]-direction parallel, the 2d-scattering pattern shows an increased intensity in horizontal direction at $q_r \approx 0.38$ Å^{-1}. Straightforwardly, the same argumentation is for the (010)-planes. Isotropically oriented crystals yield a scattering ring at the respective q-value. The orientation is analyzed by azimuthally integrating along all the orientations as depicted with the white dashed line.

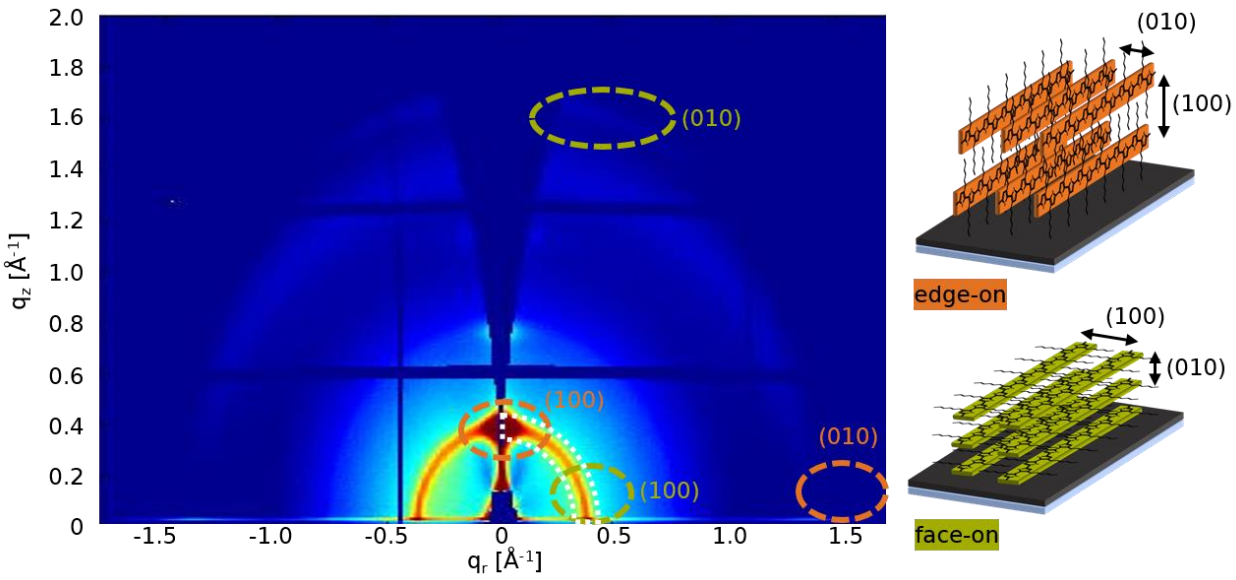

Figure S 3: Identification of crystal orientation on a 2d GIWAXS pattern. The P3HT polymer crystals exhibit typical diffraction patterns that allow to identify the orientation of the crystals. An edge-on crystal is schematically depicted in the top right corner. They exhibit a higher scattering intensity of the (100) planes in vertical direction and of the (010) peak resulting from the π-π stacking in horizontal direction. In contrast, the face-on oriented crystal (depicted in the lower bottom right corner) results in higher scattering intensities of the (100) plane in horizontal

direction and of the (010) planes in vertical direction. The white dotted semi-circle is the area on which the orientation analysis is performed (see **Figure S 4**).

The obtained azimuthal integrals for the orientation analysis are depicted in **Figure S 4** for the reference sample printed without application of an external electric field and the samples with highest forward (+100 V) and backward (-100 V) applied voltage. The intensity profiles are background corrected to account for the amorphous material. P3HT behaves as an in-plane powder, meaning, no preferred orientation in-plane occurs. To account for the amount of crystals, the obtained intensity profiles are sin(χ) corrected [6–8]. The gray area underneath the scattering curves is due to the scattering signals from the isotropically oriented crystals. The orange area at $\chi < 45°$ results from the edge-on oriented crystals and the green area at $\chi > 45°$ from the face on oriented crystals. Due to the inaccessible q-range at small azimuthal angles χ, the values are interpolated to 0 for $\chi \rightarrow 0°$.

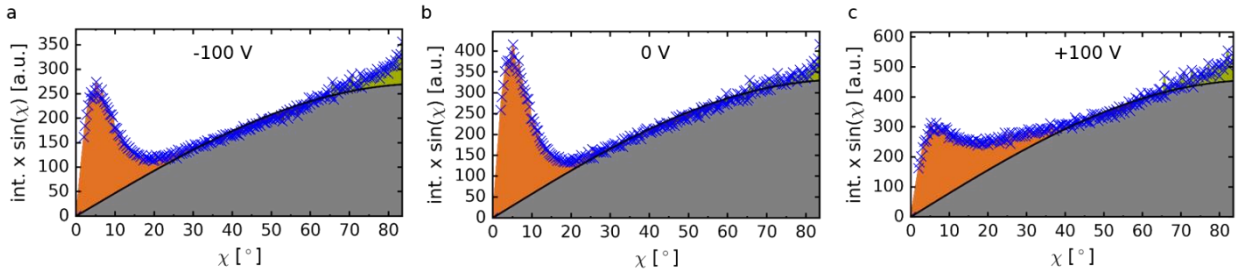

Figure S 4: Orientation analysis of an azimuthally integrated intensity profile. The intensity profiles along the azimuthal angle from 0° (vertical direction) to 85° (horizontal, positive q_r) are sin(χ) corrected due to the in-plane isotropy of the P3HT crystals [6–8]. The gray lower area represents the isotropic crystals, the orange area at low χ results from the edge-on oriented crystals and the green area at high χ from face-on crystals. Shown are the polar cuts for applied external voltages between substrate and print head/top electrode of **a** -100 V, **b** 0 V and **c** +100 V.

Information on lateral structures are obtained from horizontal line profiles of grazing incidence small angle X-ray scattering (GISAXS) data [9]. **Figure S 5**a shows the obtained horizontal line profiles for the films printed under different applied voltages obtained at the Yoneda [10] position of PCBM. The orange curves in the figure are the modeled horizontal GISAXS curves. From the models, cylindrical form and structure factors are used that are interpreted as size and corresponding distances between domains respectively. Theses domains are attributed to PCBM rich domains [4,11–13]. The extracted structure sizes are shown in **Figure S 5**b. The larger structures sizes (top of Figure S5b) slightly increase for a backward electric field while the fluctuations in the small structures (bottom of Figure S5b) do not vary outside the error bars. A forward directed electric field leads to slightly smaller structure sizes. Their respective lateral distances are depicted in **Figure S 5**c. The electric field does barely influence the lateral distances.

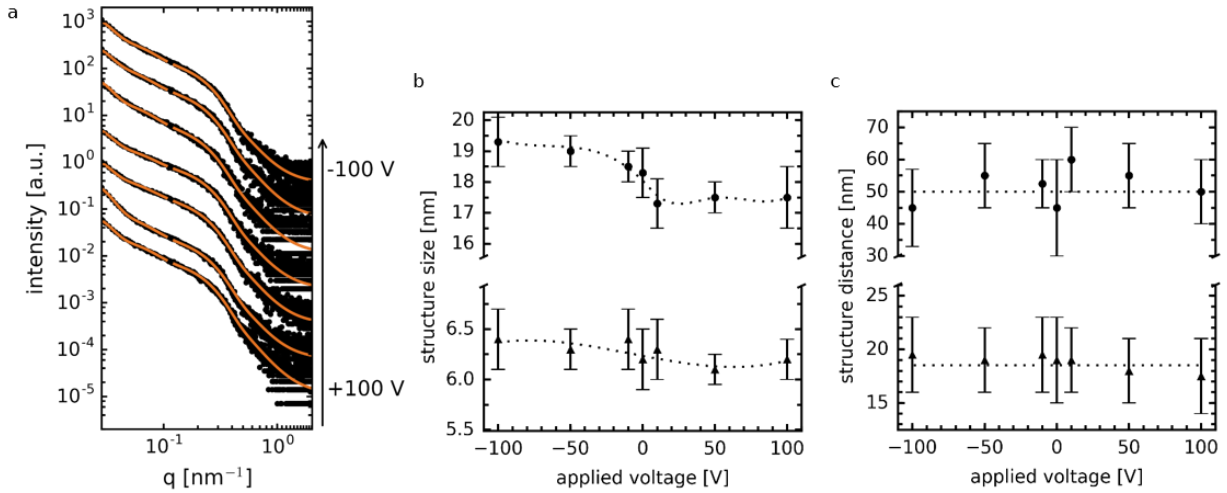

Figure S 5: Horizontal GISAXS profiles with fits and the resulting structure sizes. a, The horizontal line profiles are obtained at the Yoneda position of PCBM. The observed features originate from the lateral structures inside the film. The orange lines are the modeled data of the GISAXS cuts. **b,** The structure sizes obtained from the form factors of the fits with **c,** their corresponding structure distances obtained from the structure factors.

Insight into the vertical material composition is obtained from X-ray reflectivity (XRR) measurements. The specular reflection of the X-ray is tracked, which exhibits characteristic film properties. Depending on the distribution of scattering length densities (SLD), the X-ray beam is reflected at interfaces of different SLDs. This yields fringes, the Kissing oscillations, and a roughness dependent slope of the reflectivity data. **Figure S 6**a shows the XRR data measured for the different films, along with the fits of the vertical layer model obtained by using Motofit software [14]. Modeling the data with a layered system yields a SLD profile in vertical direction. As PCBM and P3HT exhibit differences in their SLD, the obtained profile can be converted into a material composition profile. **Figure S 6**b shows the calculated volume concentration of PCBM as a function of film depth. As for the mean SLD of the XRR fits, the mean PCBM volume concentration is the same (52 ± 1) % for all differently prepared films. The inversion of an interfacial PCBM enrichment for different directions of the electric field is deduced.

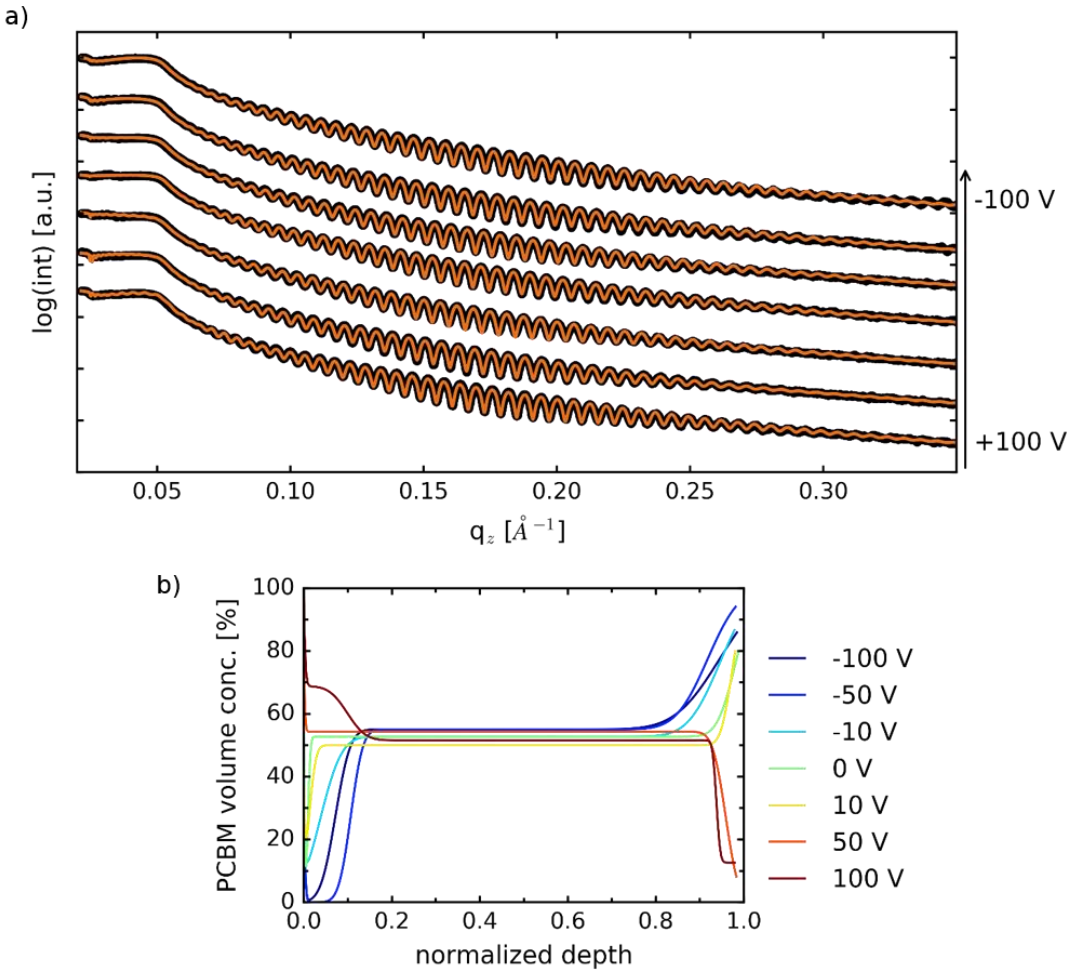

Figure S 6: X-ray reflectivity (XRR) data and deduced film roughness. a, XRR data for the different applied voltages shifted along the intensity axis for clarity. The orange line is the fit of the reflectivity data. **b,** The volume concentration of PCBM as a function of the depth in the film is derived from the scattering length densities of the XRR fits. An average of 50 % PCBM is conserved for all fits. For both images, the normalized depth 1 is the film/air interface.

Figure S 7 shows the robot setup at the beamline 7.3.3 at the Advanced Light Source (ALS) of the Lawrence Berkeley National Laboratory (LBNL). The samples are provided on separate chucks, each equipped with a bar code to identify the sample. A robot picks up the sample, passes a bar code reader and places the sample into the beam path. After the robot moved back to its home position, the alignment and measurement are started.

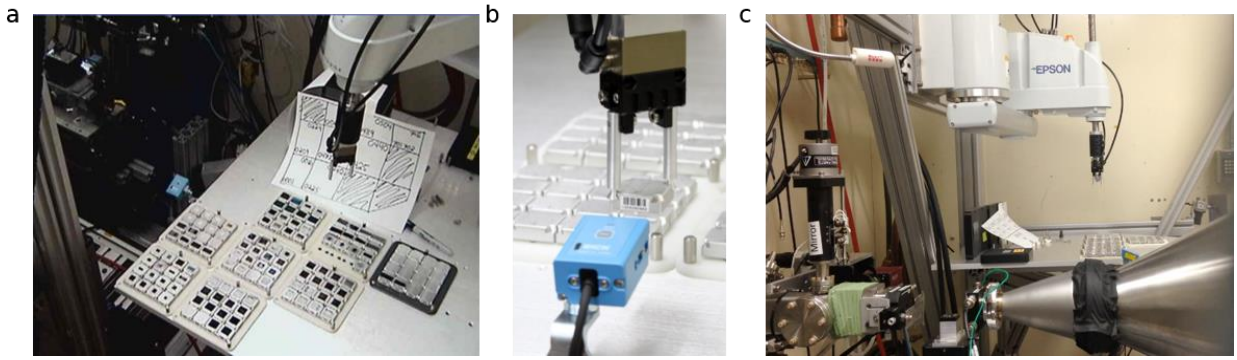

Figure S 7: Pictures of the robot used to obtain the scattering data at ALS. a, The samples are provided on sample boxes containing 4x4 chucks on which the probe is fixed. **b**, The robot picks up the chucks and a bar code scanner identifies the sample under investigation. **c**, After placing the chuck with sample to the appropriate position the robot moves back to the home position and the sample can be aligned and measured.

References

1 P. Müller-Buschbaum, *Adv. Mater.*, 2014, **26**, 7692–7709.

2 Z. Jiang, *J. Appl. Crystallogr.*, 2015, **48**, 917–926.

3 H. Sirringhaus, P. J. Brown, R. H. Friend, M. M. Nielsen, K. Bechgaard, B. M. W. Langeveld-Voss, A. J. H. Spiering, R. A. J. Janssen, E. W. Meijer, P. Herwig and D. M. de Leeuw, *Nature*, 1999, **401**, 685–688.

4 M.-Y. Chiu, U.-S. Jeng, M.-S. Su and K.-H. Wei, *Macromolecules*, 2010, **43**, 428–432.

5 S. Guo, M. A. Ruderer, M. Rawolle, V. Körstgens, C. Birkenstock, J. Perlich and P. Müller-Buschbaum, *ACS Appl. Mater. Interfaces*, 2013, **5**, 8581–8590

6 J. L. Baker, L. H. Jimison, S. Mannsfeld, S. Volkman, S. Yin, V. Subramanian, A. Salleo, A. P. Alivisatos and M. F. Toney, *Langmuir*, 2010, **26**, 9146–9151.

7 K. A. Page, A. Kusoglu, C. M. Stafford, S. Kim, R. J. Kline and A. Z. Weber, *Nano Lett.*, 2014, **14**, 2299–2304.

8 A. F. Huq, A. Ammar, A. M. Al-Enizi and A. Karim, *Polymer*, 2017, **113**, 200–213.

9 P. Müller-Buschbaum, ed. M. Gomez, A. Nogales, M. C. Garcia-Gutierrez and T.A. Ezquerra, Springer, New York, 2009, pp. 61–89.

10 Y. Yoneda, *Phys. Rev.*, 1963, **131**, 2010–2013.

11 K. W. Chou, B. Yan, R. Li, E. Q. Li, K. Zhao, D. H. Anjum, S. Alvarez, R. Gassaway, A. Biocca, S. T. Thoroddsen, A. Hexemer and A. Amassian, *Adv. Mater.*, 2013, **25**, 1923–1929.

12 S. Pröller, F. Liu, C. Zhu, C. Wang, T. P. Russell, A. Hexemer, P. Müller-Buschbaum and E. M. Herzig, *Adv. Energy Mater.*, 2016, **6**, 1501580.

13 W.-R. Wu, U.-S. Jeng, C.-J. Su, K.-H. Wei, M.-S. Su, M.-Y. Chiu, C.-Y. Chen, W.-B. Su, C.-H. Su and A.-C. Su, *ACS Nano*, 2011, **5**, 6233–6243.

14 A. Nelson, *J. Appl. Crystallogr.*, 2006, **39**, 273–276.